Biosensors and Bioelectronics 133 (2019) 100–106

Contents lists available at ScienceDirect

Biosensors and Bioelectronics

journal homepage: www.elsevier.com/locate/bios

Photoelectrochemical bioanalysis of antibiotics on rGO-Bi_2WO_6-Au based on branched hybridization chain reaction

Ruijin Zeng[a], Lijia Zhang[a], Lingshan Su[a], Zhongbin Luo[a], Qian Zhou[b,*], Dianping Tang[a,*]

[a] Key Laboratory for Analytical Science of Food Safety and Biology (MOE & Fujian Province), State Key Laboratory of Photocatalysis on Energy and Environment, Department of Chemistry, Fuzhou University, Fuzhou 350116, PR China

[b] Institute of Environmental and Analytical Science, School of Chemistry and Chemical Engineering, Henan University, Kaifeng 475004, Henan, PR China

ARTICLE INFO

Keywords:
Photoelectrochemical bioanalysis
Branched hybridization chain reaction
rGO-Bi_2WO_6-Au
Isothermal signal amplification
Multistep electron-transfer

ABSTRACT

Herein a versatile photoelectrochemical (PEC) bioanalysis platform for sensitive and specific screening of low-abundance antibiotics (kanamycin, Kana, used in this case) was innovatively designed using rGO-Bi_2WO_6-Au as photoactive matrix and target-induced branched hybridization chain reaction (t-bHCR) for efficient signal amplification. To realize the high-performance of our PEC bioanalysis system, rational introduction of reduced graphene oxide (rGO) and Au nanoparticles (Au NPs) greatly accelerated the electron transfer and enhances photoactivity. As expected, the ternary nanocomposite (i.e., rGO-Bi_2WO_6-Au) system with cascade energy level exhibited intense PEC signal responses thanks to multistep electron-transfer (MET) mechanism. Upon sensing the target Kana, t-bHCR is readily implemented, thus resulting in the assembly of numerous CuS nanoparticle (CuS NP). As a result, the loading CuS NPs from hyper-branched structure boosted the electron donors (ascorbic acid) consumption and enhanced the steric hindrance, synergistically decrease the photoelectric response. Under the optimized testing conditions, the t-bHCR-based PEC bioanalysis exhibited superior analytical performance with a linear range of 1 pM to 5 nM target Kana and limit of detection down to 0.78 pM. Additionally, favorable stability, great anti-interference ability and satisfactory accuracy for the analysis of actual samples were acquired. Impressively, the concept of t-bHCR-mediated provides an alternative to construct PEC bioanalysis and inspire more interest in the design of advanced PEC bioanalysis through nucleic acid-related signal amplification.

1. Introduction

Aptamer-based photoelectrochemical (PEC) bioanalysis on the basis of the unique sensitivity of the PEC technique, along with the target-specific bio-affinity properties of the aptamer, has spurred considerable research scrutiny (Zhao et al., 2015; Shu et al., 2018; Qiu et al., 2017; Cai et al., 2018). For example, Zhang et al. (2018) developed a novel bio-bar-code-based PEC bioanalysis coupling target-induced rolling circle amplification with enzymatic-catalytic precipitation. Zhou et al. (2018) reported high-performance magnetic-controlled PEC bioanalysis combined rGO-$BiFeO_3$ with hybridization chain reaction. Despite previous advances, there are two vital concerns for development of highly efficient PEC bioanalysis. (i) Intrinsically, obtaining limit of detection (LOD) usually correlated with advanced amplification, especially enzyme-associated signal amplification. However, the utilization of tool enzymes (polymerase or nicking) may suffer from the complexity of the experimental system (pH or temperature) and poor repeatability (easily denatured) (Wei et al., 2018; Xuan and Hsing, 2014; Bi et al., 2015). In this pursuit, the development of efficient isothermal enzyme-independent pattern is more attractive for the analysis of trace biomolecules. (ii) From the viewpoint of PEC bioanalysis development, challenges existed regarding the fast recombination of electron-hole pairs.

Hybridization chain reaction (HCR) integrated enzyme-independent, programmability and structural flexibility, has been widely applied for diverse nucleic acid-related in situ or in vitro technologies (Zeng et al., 2018a; Ren et al., 2017; Li et al., 2018). Nevertheless, conventional HCR only involve one-dimensional linear HCR, which faced the situation of insufficient amplification. Branched hybridization chain reaction (bHCR), a robust, higher-order branched nucleic acid amplification technology, coupled two split initiator with two-layer HCR and achieved exponential amplification through the resulting branched nanostructures (Chandran et al., 2013; Xu and Zheng, 2016; Choi et al., 2014). Recently, diverse schemes and protocols, on the basis of bHCR approaches, have been constructed to obtain high sensitivity

* Corresponding authors.
E-mail addresses: zhouqian@henu.edu.cn (Q. Zhou), dianping.tang@fzu.edu.cn (D. Tang).

https://doi.org/10.1016/j.bios.2019.02.067
Received 12 January 2019; Received in revised form 1 February 2019; Accepted 27 February 2019
Available online 11 March 2019
0956-5663/

platform. For instance, Liu et al. (2018) reported the application of bHCR in localizable imaging of messenger RNAs in living cells. Tang et al. (2017) constructed a fluorescence in situ hybridization based on bHCR for efficient signal amplification combining with ligase-mediated. To this end, our motivation is to explore a novel PEC bioanalysis based on bHCR-mediated signal amplification without the need of tool enzyme participation.

Bi_2WO_6 (BWO), Aurivillius-related semiconductor, has evoked extensive attention because of its intrinsic physical and chemical properties, e.g., excellent photon absorptivity, high PEC activity, ferroelectric piezoelectricity and so forth (Zhang et al., 2014). Like other mono-component photocatalyst, unfortunately, the unavoidable rapid recombination of photogenerated electron-hole pairs in BWO deteriorated the photocatalytic and restricted its extensive applications. To circumvent these obstacles, increasing efforts have been made to enhance PEC performance of BWO through constructing binary heterojunction (Cao et al., 2018), ion doping (Wang et al., 2018) and cocatalysts loading (Zhao et al., 2019). Among these, the BWO-based binary heterojunction composites with specific morphology, via anchoring 2D monolayer rGO to BWO (i.e. rGO-BWO), possessed improved PEC activity (Dong et al., 2017). However, such binary heterojunction only provided single electron transfer pathway, which incompetent to restrain photoinduced carrier recombination absolutely. Alternatively, it is promising to construct a multistep electron-transfer (MET) system by reasonably designed ternary composites with cascade energy level arrangement, which aim at modulated photo-induced carriers through MET. For the sake of improving sensitivity of the PEC bioanalysis platform, Au NPs and rGO are coupled with BWO in sequence (rGO-BWO-Au). Here, Au NPs and rGO provided an appropriate platform for electron acceptance and stepwise band-edge levels [BWO (−0.41 V *vs* NHE) → rGO (−0.08 V *vs* NHE) → Au (0.25 V *vs* NHE)], which further enhanced carrier separation by capturing and transferring electrons (Ning et al., 2018; Min and Lu, 2011; Xiong et al., 2010).

Kanamycin (Kana), an aminoglycoside-type antibiotic agent, displayed bactericidal activity against Gram-negative or certain Gram-positive pathogens in pharmaceutical industry, food manufacturing and animal agriculture (Furusawa et al., 2018). Accumulating evidences has demonstrated that overuse of Kana is closely related to development of multi-resistant pathogenic bacteria and other detrimental effects (Zeng et al., 2018b). Therefore, development of methodology for robust and highly sensitive antibiotics residues in agricultural products has become imperative. Herein, a newly high-performance PEC bioanalysis platform is exploited based on rGO-BWO-Au by coupling with t-bHCR for detection of Kana (Fig. S1, Scheme 1). Specifically, the Kana initially reacted with the domains of pre-hybridization Apt-c-DNA duplex to release the c-DNA. Then the free c-DNA partially hybridized with the hairpin DNA0 (H0) on the the surface of rGO-BWO-Au electrode. Thereafter, the unpaired of c-DNA propagated the 1st HCR between two metastable CuS nanoparticle-labeled hairpin DNA (CuS-HP1, CuS-HP2), yielding linear high-molecular-weight alternating copolymer with much split sequence. Subsequently, these split sequence acted as new toehold to trigger downstream 2nd HCR between another two metastable CuS nanoparticle-labeled hairpin DNA (CuS-HP3, CuS-HP4), resulting in chain-branching growth of fractal dendrimers with numerous CuS NPs incorporation. Since numerous CuS NPs competed with rGO-BWO-Au for consuming of hole-trapping agent (ascorbic acid), the photocurrent response is strikingly decreased. Moreover, in comparison to reducing photocurrent merely by competitive consumption effect of CuS NPs, the formation of hyper-branched structure further lessened the generation of photocurrent through obstructed the transmission of ascorbic acid and blocked the light irradiation to the surface of rGO-BWO-Au.

2. Experimental section

The detailed description of chemical and reagent, preparation of BWO, rGO-BWO, BWO-Au and rGO-BWO-Au, preparation of CuS NPs and hairpin DNA-CuS NPs conjugates, fabrication of PEC bioanalysis platform, analysis of real milk sample and optimization of experimental method were supplied in Supplementary material (Please see Supplementary material).

2.1. Bioanalysis for target Kana and PEC measurement

In this assay, the amine groups on hairpin DNA (H1, H2, H3 and H4) were covalently conjugated onto TGA-stabilized carboxylated CuS NPs through typical carbodiimide coupling, whereas gold nanoparticles-functionalized rGO-BWO heterojunction was fabricated via a facile hydrothermal approach and photo-reduction route in sequence. The as-prepared rGO-BWO-Au heterojunction and H0 were modified onto a cleaned FTO electrode (conductive side) through physical adsorption and strong Au-S bond (See the details in the Supporting information). Following that, target-assisted bHCR reaction was performed as follows: (i) Apt-c-DNA at a concentration of 10 μM was prepared through mixing and annealing Kanamycin-base aptamer (Apt; 10 μL, 100 μM) with equimolar level complementary DNA (c-DNA; 10 μL, 100 μM) in reaction buffer (80 μL, 10 mM PBS, 200 mM NaCl, 10 mM $MgCl_2$, pH 7.4) for 90 min; (ii) subsequently, Apt-c-DNA (final concentration 5 μM) was employed for the reaction of variety concentration of target Kana standards in the presence CuS-H1 (2.0 μM), CuS-H2 (2.0 μM), CuS-H3 (2.0 μM) and CuS-H4 (2.0 μM) on rGO-BWO-Au-modified FTO electrode in ambient air, and incubated for 3 h to fulfill the t-bHCR. Following

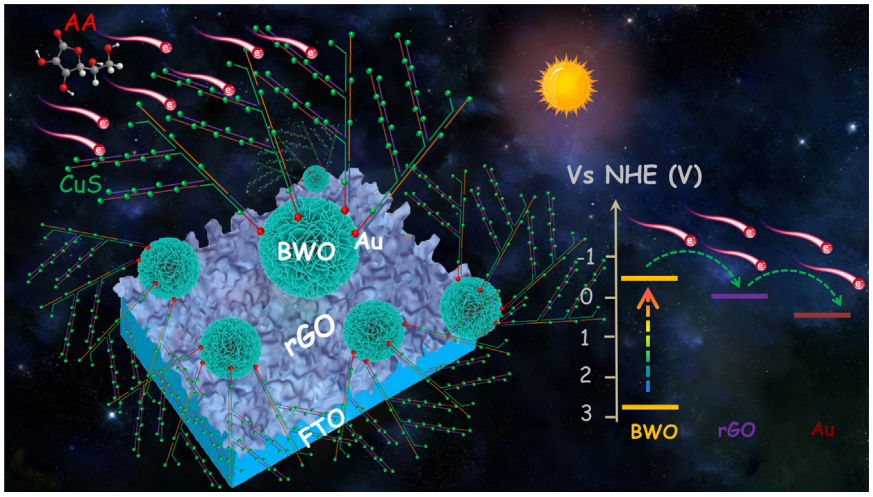

Scheme 1. Schematic illustration of target-assisted branched hybridization chain reaction (t-bHCR)-based photoelectrochemical bioanalysis toward Kanamycin (Kana) by using reduced graphene oxide-Bi_2WO_6-gold nanoparticle (Au) as the photoactive materials (rGO: reduced graphene oxide; Au: gold nanoparticle; BWO: Bi_2WO_6; AA: ascorbic acid; CuS: copper sulphide nanoparticle).

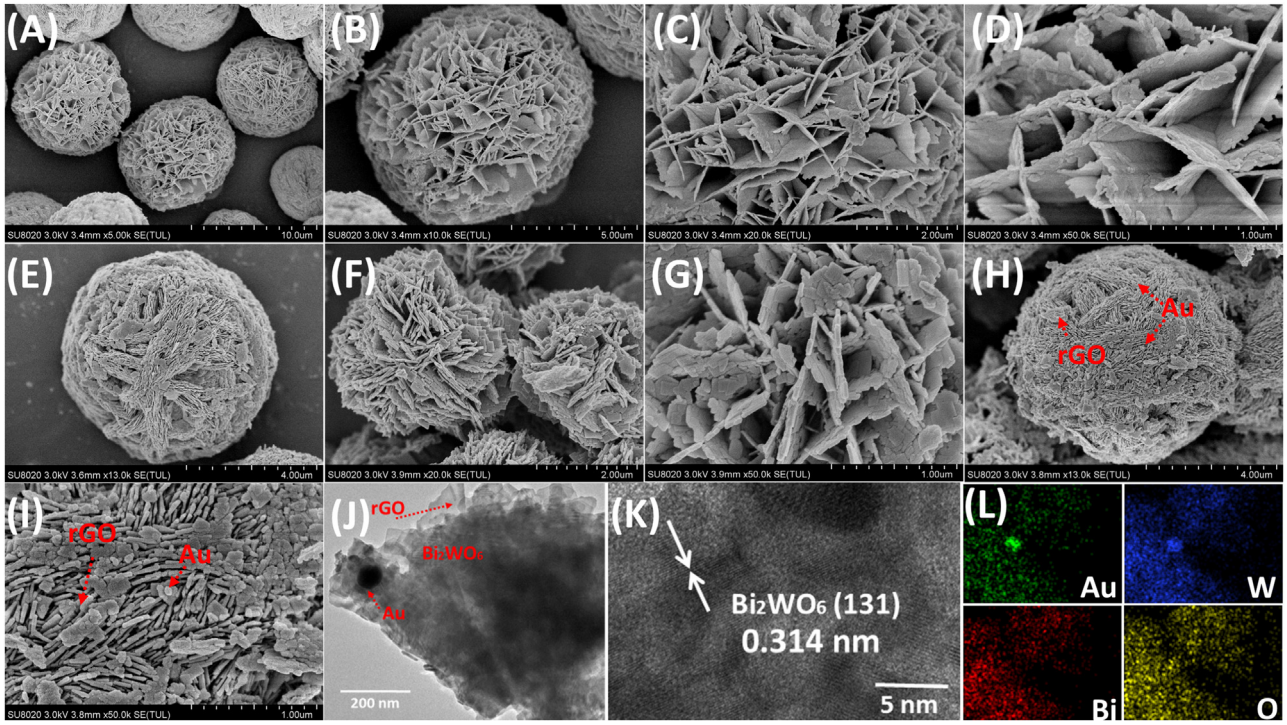

Fig. 1. (A-D) SEM images of tremella-like BWO (images with different magnifications); (E-G) SEM images of rGO-BWO (images with different magnifications); (H, I) SEM images of rGO-BWO-Au (images with different magnifications); (J, K) HRTEM image of rGO-BWO-Au; and (L) HAADF-STEM image and element mapping for Au, W, Bi and O of rGO-BWO-Au.

that, the obtained electrode was carefully rinsed with reaction buffer to eliminate excess CuS-hairpin DNA. Finally, the transient photocurrent responses were recorded in 5.5 mL of PBS solution system (0.1 M, pH 7.4, 250 mM ascorbic acid) at a constant potential of 0 V (versus Ag/AgCl) on an AutoLab-electrochemical workstation (μAutIII.Fra2.v, Netherlands) using a 500-W xenon lamp (420 nm cutoff filter, NBET) as irradiation light source (duration: 10000 ms) with home-built three-electrode cell (i.e., rGO-BWO-Au-modified FTO working electrode, a coiled Pt-wire counter electrode and Ag/AgCl reference electrode in saturated KCl solution). To verify the truth of the photocurrent data, each measurement was done in triplicate and taking the average.

3. Results and discussion

3.1. Detailed characterization of BWO, rGO-BWO, rGO-BWO-Au and CuS-hairpin DNA

The intrinsic morphology and microstructures of as synthesized pristine BWO, rGO-BWO and rGO-BWO-Au were subjected to scanning electron microscopy (SEM; JEOL, JSM-6500F, Japan). As shown in Fig. 1A-D, the low-magnification SEM images of bulk BWO presented well-defined tremella-like architecture, which was composed of numerous crisscross curly nanosheets. While the higher-magnification SEM images exhibited multilayered architectures with an average diameter of ~7.6 μm and thickness of ~6 nm. Noticeably, compared with pristine BWO, several highly transparent nanosheets were strongly integrated with the edge of BWO when rGO was introduced in hydrothermal synthesis process (Fig. 1E-G), suggesting the successfully loading of rGO onto the surface of BWO microsphere. Analogously, after benign UV-assisted photo-reduction route, a considerable part Au nanoparticles adhered to the surface of rGO-BWO in different magnification SEM images (Fig. 1H, I). The morphology and microstructure of rGO-BWO-Au was further validated by high-resolution TEM (HRTEM; JEOL, JEMARM200FTH) image (Fig. 1J). HRTEM image demonstrated the hierarchical rGO-BWO-Au consisted of BWO with good lattice, black spherical Au and flake-like rGO, indicating that rGO and Au NPs have been attached onto the surface of BWO to form rGO-BWO-Au heterojunction structure. In addition, the interval of the lattice distance was measured to be 0.314 nm, corresponding well to the spacing of (131) crystallographic planes of BWO in rGO-BWO-Au (Fig. 1K) (Zhuo et al., 2013). To verify the element composition of fabricated rGO-BWO-Au, the hierarchical rGO-BWO-Au was also studied by energy dispersive spectrometry (EDS) element mappings (Fig. 1L, Fig. S2). The elemental mapping analysis of the hierarchical rGO-BWO-Au were recorded that the coexistence and homogeneous dispersion of Au (green), Bi (red), W (blue) and O (yellow) elements throughout the whole of the nanostructure, indicating rGO and Au NPs uniformly grow on the surface of BWO. These results suggested the building units of the hierarchical rGO-BWO-Au were packed in highly ordered manner.

Except for characterizing the morphology of rGO-BWO-Au, more detailed regarding their crystallinity, chemical bond composition and surface chemical valence were further investigated. As depicted in Fig. 2A, powder X-ray diffraction (XRD; Bruker D8-Discover, Germany) patterns containing pristine BWO (curve 'a'), rGO-BWO (curve 'b') and rGO-BWO-Au (curve 'c') at a scanning rate of 7° min^{-1} in the 2 theta range from 15° to 65°. The pristine BWO displayed five primary diffraction peaks at 28.24°, 33.04°, 47.26°, 55.94°, and 58.68° matched well with the (131), (002), (260), (331) and (262) plane of standard orthorhombic BWO (JCPDS file 39-0256) without any impurity peaks, suggesting high crystalline quality of orthorhombic BWO phase. Notably, in curve 'b' and curve 'c', diffraction peaks belonging to rGO are not detected in the rGO-BWO and rGO-BWO-Au nanocomposites, probably due to the relatively low-crystallization quality and uniform dispersion (Dong et al., 2017). Significantly, except for the diffraction peaks from the rGO-BWO, another two new diffraction peaks appeared at 38.18° and 44.42° after formation of rGO-BWO-Au, which were easily assigned to the (111) and (200) planes of Au NPs (JCPDS file 80–0019), respectively. Next, Raman spectroscopy (Renishaw, 532 nm solid laser, U.K.) were recorded to further confirm the molecular structures within the range of 200–1700 cm^{-1} (Fig. 2B). For the pristine BWO (curve 'a'),

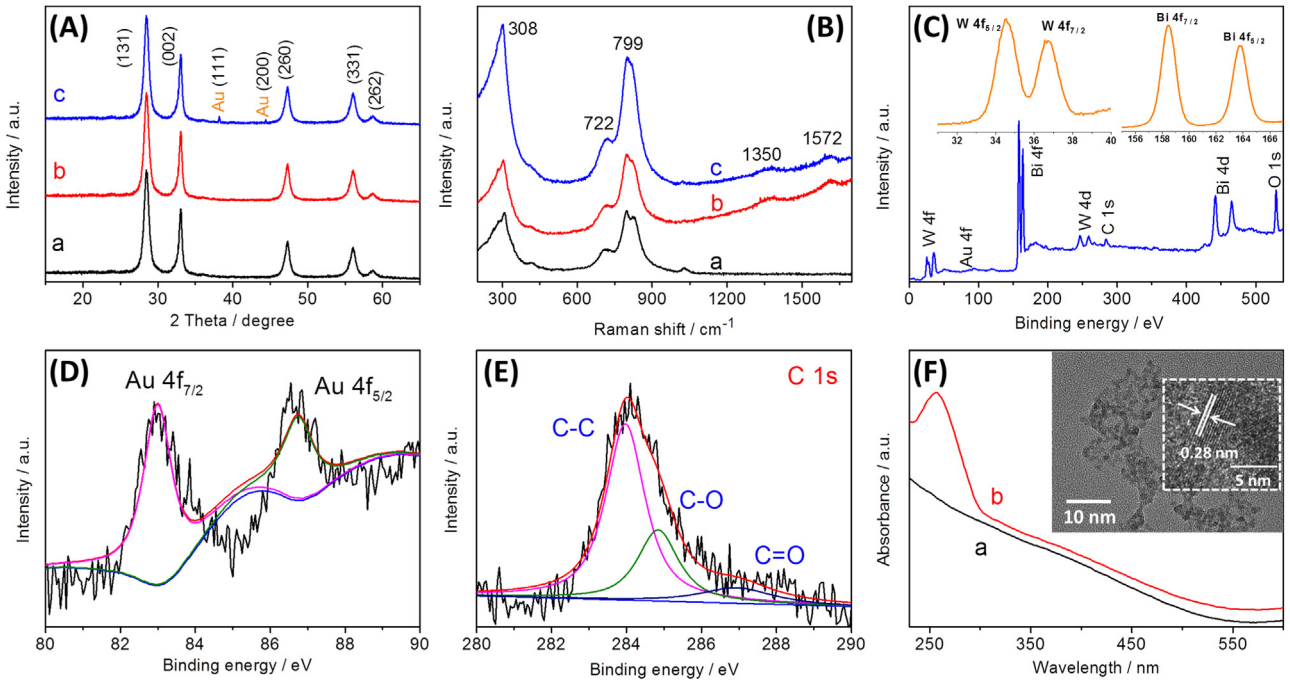

Fig. 2. (A) XRD patterns of (a) BWO, (b) rGO-BWO and (c) rGO-BWO-Au; (B) Raman patterns of (a) BWO, (b) rGO-BWO and (c) rGO-BWO-Au; XPS survey spectra of (C) rGO-BWO-Au [inset: high-resolution XPS spectra of W 4f and Bi 4f]; (D) Au 4f and (E) C 1s; (F) UV–Vis absorption spectra of (a) CuS NPs and (b) CuS-hairpin DNA (inset: HRTEM image of CuS NPs).

three distinguishable Raman bands centered around at 308 cm^{-1}, 722 cm^{-1} and 799 cm^{-1}, allotted to stretching or bending vibrations of the Bi-O bond, antisymmetric bridging mode of tungstate chain and A_g mode of O-W-O in WO_6 octahedral, respectively (Yang et al., 2017). As expected, the spectrum of the as-prepared rGO-BWO (curve 'b') and rGO-BWO-Au (curve 'c') displayed another two typical low-intensity peaks at 1350 cm^{-1} (D band) and 1572 cm^{-1} (G band), which could be explained by the successful coating of rGO on BWO nanosheets. To get an insight into the atom valence states and electronic interaction between BWO, RGO and Au in the composites, X-ray photoelectron spectroscopy (XPS; Thermo Fisher, USA, the peak of calibrated carbon at 284 eV) was further inspected. As shown from XPS survey spectrum in Fig. 2C, all elements valences (Bi 4f, 4d; W 4f; O 1s; Au 4f and C 1s) related to BWO, rGO and Au NPs can be observed in rGO-BWO-Au. The binding energies of W $4f_{7/2}$ and W $4f_{5/2}$ are 34.55 and 36.85 eV in the rGO-BWO-Au (Fig. 2C, top left inset), which can be attributed to the hexavalent W^{6+} state existing in the composites (Liu et al., 2016). Similarly, the spin-orbit components of two individual peaks situated at 158.5 and 163.85 eV (Fig. 2C, top right inset), corresponding to Bi^{3+} $4f_{7/2}$ and Bi^{3+} $4f_{5/2}$ in rGO-BWO-Au, respectively (Tian et al., 2013). Meanwhile, the Au 4f of the rGO-BWO-Au also presented the characteristic double signals at 83.00 (Au $4f_{7/2}$) and 86.75 eV (Au $4f_{5/2}$) by Gauss fitting, confirming the existence of Au^0 state (Fig. 2D). Besides, the C 1s peak of rGO-BWO-Au was reasonably fitted with three component peaks located at 284.0, 284.9 and 287.0 eV (Fig. 2E), corresponding to sp^2-hybridized carbon species in aromatic rings (C-C/C=C), epoxy or alkoxy carbon (C-O) and carboxylic carbon (C=O), respectively (Ma and Tsukruk, 2017). Overall, based on the aforementioned results from SEM, HRTEM, EDS element mapping, XRD, Raman and XPS, we might conclude that heterojunction could be successfully construction via facile hydrothermal approach and photo-reduction route in sequence.

The sensitivity of t-bHCR-based PEC platform is directly related to the competitive ability of the CuS NPs involved. Accordingly, the successful preparation of CuS NPs and CuS-hairpin DNA were also very crucial. The HRTEM image of the TGA-stabilized CuS NPs exhibited monodisperse crystalline with an average size around 7.2 nm (Fig. 2F, inset). Meanwhile, the well-resolved characteristic lattice fringe for the (006) plane of CuS NPs could be clearly observed with the inter-planar spacing of ~0.28 nm (Fig. 2F, inset) (Wang et al., 2016). Furthermore, the TGA-stabilized CuS NPs and bio-conjugation of CuS NPs with hairpin DNA were monitored by UV–vis absorption spectroscopy (Tecan Infinite 200 Pro, 230–600 nm, Switzerland) (Fig. 2F). The CuS NPs showed strong optical absorption at UV–vis region (curve 'a'), indicating it could competitively absorb light with the rGO-BWO-Au photoactive materials. Comparatively, when the CuS NPs was decorated on hairpin DNA by typical carbodiimide reaction, there was a characteristic absorption peaks for CuS-hairpin DNA at 260 nm (curve 'c'), indicating the CuS NPs has been successfully labeled on the hairpin DNA probe.

3.2. Feasibility investigation and control tests

As aforementioned above, the change in the photocurrent value on rGO-BWO-Au derived from the t-bHCR-based products. Thus, one inevitable question arises as to whether the system could be readily implemented with the t-bHCR reaction. To clarify this point, polyacrylamide gel electrophoresis (PAGE, 12% gel, 1 h at 90V) was first applied to evaluate the t-bHCR amplifier for Kana assay without the labeling of CuS NPs (Fig. 3A). Lanes 'a-f ' gave clearly PAGE images of H0, H1, H2, H3, H4 and Apt-c-DNA, respectively. When the Apt-c-DNA reacted with H0 in the presence of 5 nM target Kana, a weak strip for the hybridized H0-c-DNA structures was appeared at the top of lane 'g' in addition to those of excess Apt-c-DNA (middle) and H0 (bottom). Upon addition the mixture of H1 and H2 into lane 'g'-based system, as anticipated, a series of gradient band were obtained in lane 'h' system, which indicating the self-assembly of the HCR product spontaneously. Moreover, the similar phenomena could be found in lane 'i' when H3 and H4 were present in the lane 'h'-based system. However, the above PAGE images results did not show the difference between liner-HCR and bHCR, thus lengthen the electrophoresis time to observe their differences. After longer electrophoresis time (6 h at 90 V), lane 'i' with little mobility was observed in comparison with lane 'h', which ascribed to the formation of the bHCR structure with larger steric hindrance and

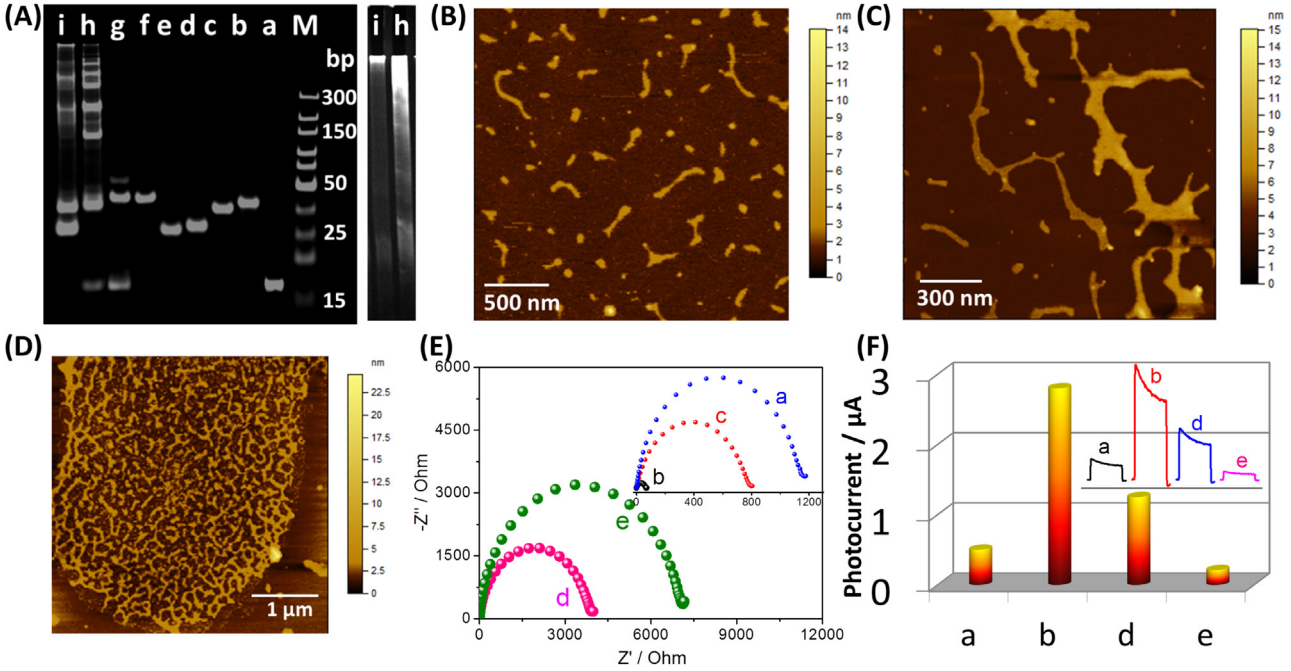

Fig. 3. (A) PAGE (12% gel) for different samples (lane M: 300 bp-DNA marker; lane 'a-e': H0-H4; lane 'f': Apt + c-DNA; lane 'g': lane f + Kana + H0; lane 'h': lane g + H1 + H2; lane 'i': lane h + H3 + H4); right inset: after long electrophoresis time PAGE image; AFM images of (B) lane 'h'; (C-D) lane 'i'; (E) Nyquist diagrams of (a) BWO, (b) rGO-BWO-Au, (c) rGO-BWO-Au-H0, (d) rGO-BWO-Au-H0 + Apt + c-DNA + Kana + H1 + H2, and (e) rGO-BWO-Au-H0 + Apt + c-DNA + Kana + H1 + H2 + H3 + H4 in PBS (10 mM, pH 7.4) containing 5 mM $Fe(CN)_6^{4-/3-}$ and 0.1 M KCl; (F) Photocurrent value of (a, b, d, e) mentioned in part E. (concentrations of Kana, Apt, c-DNA, H0, H1, H2, H3 and H4 were 5 nM, 5 μM, 5 μM, 2 μM, 2 μM, 2 μM, 2 μM and 2 μM, respectively).

molecular weight. Therefore, the PAGE gel images successful confirm the proposed t-bHCR took place as anticipated. Beyond that, the PAGE results and envisaged morphology of the bHCR product were further confirmed by direct imaging in atomic force microscopy (AFM; Nanoscope, Bruker). A linear, one-dimensional polymer wires with a majority of 50–500 nm in length were observed in the product of lane 'h' (Fig. 3B). Instead, plenty of two-dimensional highly-branched morphology with great dispersity were appeared in the product of lane 'i' (Fig. 3C-D). These AFM images gave clear evidences for branched assembly in the bHCR and in accordance with the PAGE gel.

Certainly, another puzzling question is whether the t-bHCR-based system successfully established and further employed for the PEC Kana-detection. In this regard, electrochemical impedance spectroscopy (EIS, frequency range from 0.01 Hz to 10 kHz) and time-photocurrents were applied to monitor the state of each electrode modification process. Intrinsically, the semicircle portion of EIS Nyquist plots at higher frequencies represented electron-transfer process. Typically, different from pristine BWO-modified FTO (Fig. 3E, Nyquist 'a' and Fig. 3F, curve 'a'), rGO-BWO-Au-modified FTO exhibited the highest density of photocurrents and smallest resistance (Fig. 3E, Nyquist 'b' and Fig. 3F, curve 'b'), revealing best electrical conductivity and superior PEC properties via MET channel. In detail, Au NPs and rGO could improve the charge separation of carriers via Schottky barrier formation, surface plasmon resonance and high electron mobility (Shu et al., 2018; Zhou et al., 2018). Subsequently, the resistance gradually increased when H0 and MCH were assembled to the rGO-BWO-Au/FTO, owing to the repelling effect of negatively oligonucleotides toward $Fe(CN)_6^{3-/4-}$ (Fig. 3E, Nyquist 'c'). Furthermore, with the progression of HCR procedure between H1 and H2, the formed long HCR structure with numerous CuS NPs increased resistance and reduced photocurrent to some extent (Fig. 3E, Nyquist 'd' and Fig. 3F, curve 'd'). During this process, the increase resistance on account of the enhanced repulsion effect of the negatively charged phosphate backbone and the $Fe(CN)_6^{3-/4-}$, while the decrease in photocurrent owing to the synergistic effect of steric hindrance and the consumption of ascorbic acid by CuS NPs. For the same reason, the trend described above is further enhanced (Fig. 3E, Nyquist 'e' and Fig. 3F, curve 'e'). It is worth to point out that the bHCR-based photocurrent signal is ~5.9 folds lower than the HCR-based, indicating bHCR as effective signal amplification ameliorated the PEC performance.

3.3. Analytical performance of t-bHCR-Based rGO-BWO-Au PEC bioanalysis platform

By coupling t-bHCR-based signal amplification with rGO-BWO-Au PEC bioanalysis platform, variable concentrations of Kana standards were systematically tested under the optimized reaction circumstance (Fig. S4). The photocurrent decreased linearly with continuously increased the target Kana concentration (Fig. 4A). A preferable linear-dependence photocurrent-time decay curves was acquired in the detection range from 1.0 pM to 5.0 nM Kana, and the corresponding regression equation was I (μA) = 2.5295 – 0.629 × $\log C_{[Kana]}$ (pM, R^2 = 0.9903, n = 7) (Fig. 4B). The LOD value was calculated to be 0.78 pM at $3S_B$ principle (S_B expressed as the standard deviation of the 11-blank sample, IUPAC method, 1978). Clearly, the LOD value in this method was much lower than the maximum residual limits standard of the European Union (150 μg kg^{-1}, ≈ 257.5 nM) and China (200 μg kg^{-1}, ≈ 343.3 nM). To further illustrate the merits of t-bHCR-based rGO-BWO-Au PEC bioanalysis platform, the LOD value of this strategy was compared with recently reported Kana-schemes (Table S1 in the Supporting information). Distinctly, here the as-proposed strategy for Kana assay could display superior sensitivity, which mainly ascribed to smart integration of the rGO-BWO-Au photoactive matrix and t-bHCR-mediated signal amplification endowing the platform with ultrasensitive photocurrent readout. Moreover, the relative standard deviation (RSDs) were 5.94%, 5.13%, 5.99% and 5.52% (n = 4) for intra-assays, and 9.21%, 9.75%, 10.05% and 9.66% (n = 4) for inter-assays toward 50 pM, 500 pM, 1 nM and 5 nM target Kana, respectively, undoubtedly demonstrating good assay precision and desirable reproducibility. Additionally, as the photocurrent-generation tag in this

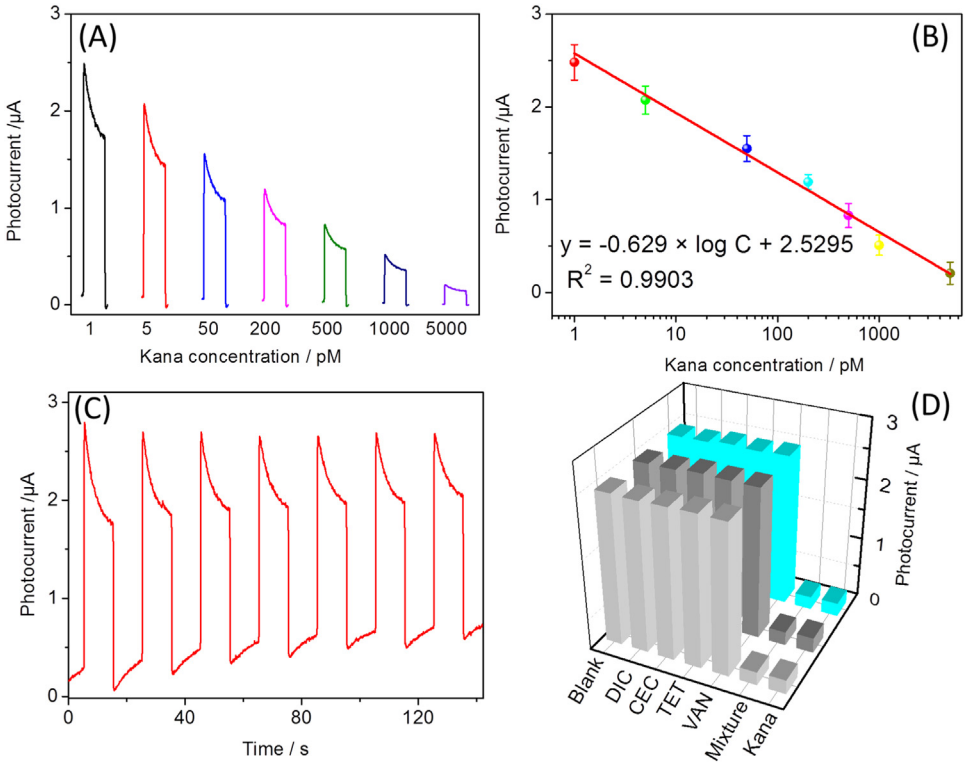

Fig. 4. (A) Photocurrents of t-bHCR-based rGO-BWO-Au PEC bioanalysis platform toward target Kana; (B) calibration plots between photocurrent (μA) and the logarithm of Kana concentration (pM), error bars = SD (n = 3); (C) time-dependence photocurrents curve on rGO-BWO-Au/FTO electrode under seven 'on-off' irradiation for 140 s; and (D) the anti-interference ability against 5.0 nM Kana, 500 nM dicloxacillin (DIC), 500 nM cefaclor (CEC), 500 nM tetracycline hydrochloride (TET), 500 nM vancomycin hydrochloride (VAN) and the mixture containing the aforementioned analytes.

system, the stability of the rGO-BWO-Au/FTO electrode was recorded within seven repeated 'on-off' light irradiation (Fig. 4C). The photocurrent response and peak shape revealed little fluctuation during this period (RSD = 1.68%), suggesting the excellent stability of photocurrent readout. As an essential parameter for PEC sensing, the specificity of t-bHCR-based rGO-BWO-Au PEC bioanalysis platform should further systematically estimate. Other common antibiotics species in the market, namely, dicloxacillin (DIC), cefaclor (CEC), tetracycline hydrochloride (TET) and vancomycin hydrochloride (VAN) were introduced as control. These non-targets antibiotics analytes (500 nM) were separately measured, and then their mixture (containing 5.0 nM Kana and 500 nM non-targets antibiotics analytes) were determined under the same condition. As presented in Fig. 4D, apart from the photocurrent responses of Kana alone and the mixture containing Kana displayed significantly decreased, all other non-targets antibiotics analytes and blank sample exhibited relatively high intensities. The aforementioned results indicated that t-bHCR was exclusively initiated by the Kana and the high selectivity of t-bHCR-based rGO-BWO-Au PEC bioanalysis.

3.4. Screening of actual milk samples

For further evaluated the practical applicability of the t-bHCR-based rGO-BWO-Au PEC bioanalysis platform for Kana detection in actual complex samples, qualified milk from local Walmart supermarket spiked with different-level Kana standards. Additionally, the target Kana levels in six spiking samples were assayed in comparison with commercial available Kana ELISA rapid diagnostic kit (Beijing Clover Technology Group Inc.). The correlation between the two methods (t-bHCR-based PEC method and Kana ELISA kit) was evaluated according to the student's *t*-test formula. The obtained results were tabulated in Table 1 as mean ± SD (RSD %). All t_{exp} values for six samples were below 2.776 at the 95% confidence level ($t_{crit[0.05,4]}$ = 2.776), thereby revealing well-matched precision between two methods.

Table 1
Screening of milk using t-bHCR-based PEC method and Kana ELISA kit.

sample no.	method; concentration: mean ± SD (nM, *n* = 3) (RSD%)		t_{exp}
	t-bHCR-based PEC	Kana ELISA kit	
1	0.52 ± 0.02 (2.92%)	0.49 ± 0.03 (6.12%)	1.72
2	1.04 ± 0.06 (6.38%)	0.99 ± 0.07 (7.07%)	0.95
3	1.98 ± 0.02 (1.05%)	1.96 ± 0.06 (2.91%)	0.67
4	3.03 ± 0.04 (1.19%)	3.00 ± 0.03 (1.02%)	1.22
5	3.98 ± 0.14 (3.61%)	4.06 ± 0.11 (2.74%)	0.82
6	4.97 ± 0.15 (3.02%)	4.93 ± 0.16 (3.32%)	0.31

4. Conclusions

In conclusion, this contribution successfully devised an advanced PEC bioanalysis platform for the determination of antibiotic (Kanamycin, Kana used as model analyte) by coupling with rGO-BWO-Au and t-bHCR for the signal amplification. Relative to traditional PEC bioanalysis strategies, two overwhelming advantages offered by our work should be emphasized. Above all, the t-bHCR enabled to generate a hyper-branched assembly with numerous CuS NPs incorporation from molecular recognition event for a short time, thus resulting in the exponential amplification. Second, ternary nanocomposite rGO-BWO-Au with cascade energy level (BWO→ rGO→ Au) can effortlessly block the charge recombination through multistep electron-transfer (MET) mechanism. In particular, our system offers a new perspective for fabrication of high-performance PEC bioanalysis platform by using nucleic acids as amplification indicators. Nevertheless, one major shortcoming of our strategy involves five hairpins DNA for the construction of system. Therefore, follow-up study should be focused on improvement of the bioanalysis platform.

CRediT authorship contribution statement

Ruijin Zeng: Investigation, Writing - original draft. **Lijia Zhang:** Conceptualization, Writing - review & editing. **Lingshan Su:** Formal analysis. **Zhongbin Luo:** Data curation. **Qian Zhou:** Software. **Dianping Tang:** Methodology, Supervision.

Acknowledgments

Authors acknowledged financial support from the National Natural Science Foundation of China (Grant nos.: 21675029 & 201874022) and the Health-Education Joint Research Project of Fujian Province (Grant no.: WKJ2016-2-15).

Credit author statement

I would like to declare on behalf of my co-authors that the work described was original research that has not been published previously, and not under consideration for publication elsewhere, in whole or in part.

Declaration of interests

None.

Appendix A. Supplementary material

Supplementary data associated with this article can be found in the online version at https://doi.org/10.1016/j.bios.2019.02.067.

References

Bi, S., Chen, M., Jia, X., Dong, Y., Wang, Z., 2015. Angew. Chem. Int. Ed. 54, 8144–8148.
Cai, G., Yu, Z., Ren, R., Tang, D., 2018. ACS Sens. 3, 632–639.
Cao, S., Shen, B., Tong, T., Fu, J., Yu, J., 2018. Adv. Funct. Mater. 28, 1800136.
Choi, H., Beck, V., Pierce, N., 2014. ACS Nano 8, 4284–4294.
Chandran, H., Rangnekar, A., Shetty, G., Schultes, E.A., Reif, J.H., LaBean, T.H., 2013. Biotechnol. J. 8, 221–227.
Dong, S., Ding, X., Guo, T., Yue, X., Han, X., Sun, J., 2017. Chem. Eng. J. 316, 778–789.
Furusawa, C., Horinouchi, T., Maeda, T., 2018. Curr. Opin. Biotechnol. 54, 45–49.
Li, J., Liu, S., Sun, L., Li, W., Zhang, S., Yang, S., Li, J., Yang, H., 2018. J. Am. Chem. Soc. 140, 16589–16595.
Liu, Y., Chen, L., Yuan, Q., He, J., Au, C., Yin, S.F., 2016. Chem. Commun. 52, 1274–1277.
Liu, L., Liu, J., Wu, H., Wang, X., Yu, R., Jiang, J., 2018. Anal. Chem. 90, 1502–1505.
Ma, R., Tsukruk, V., 2017. Adv. Funct. Mater. 27, 1604802.
Min, S., Lu, G., 2011. J. Phys. Chem. C 115, 13938–13945.
Ning, X., Li, W., Meng, Y., Qin, D., Chen, J., Mao, X., Xue, Z., Shan, D., Devaramani, S., Lu, X., 2018. Small 14, 1703989.
Qiu, Z., Shu, J., Tang, D., 2017. Anal. Chem. 90, 1021–1028.
Ren, K., Xu, Y., Liu, Y., Yang, M., Ju, H., 2017. ACS Nano 12, 263–271.
Shu, J., Qiu, Z., Lv, S., Zhang, K., Tang, D., 2018. Anal. Chem. 90, 2425–2429.
Tian, J., Sang, Y., Yu, G., Jiang, H., Mu, X., Liu, H., 2013. Adv. Mater. 25, 5075–5080.
Tang, Y., Zhang, X., Tang, L., Yu, R., Jiang, J., 2017. Anal. Chem. 89, 3445–3451.
Wang, L., Wang, Z., Zhang, L., Hu, C., 2018. Chem. Eng. J. 352, 664–672.
Wang, Z., Tang, X., Wang, X., Yang, D., Yang, C., Lou, Y., Chen, J., He, N., 2016. Chem. Commun. 52, 12210–12213.
Wei, J., Gong, X., Wang, Q., Pan, M., Liu, X., Liu, J., Xia, F., Wang, F., 2018. Chem. Sci. 9, 52–61.
Xiong, Z., Zhang, L., Ma, J., Zhao, X., 2010. Chem. Commun. 46, 6099–6101.
Xu, Y., Zheng, Z., 2016. Biosens. Bioelectron. 79, 593–599.
Xuan, F., Hsing, I., 2014. J. Am. Chem. Soc. 136, 9810–9813.
Yang, J., Chen, D., Zhu, Y., Zhang, Y., Zhu, Y., 2017. Appl. Catal. B: Environ. 205, 228–237.
Zeng, R., Su, L., Luo, Z., Zhang, L., Lu, M., Tang, D., 2018a. Anal. Chim. Acta 1038, 21–28.
Zeng, R., Luo, Z., Zhang, L., Tang, D., 2018b. Anal. Chem. 90, 12299–12306.
Zhang, K., Lv, S., Lin, Z., Li, M., Tang, D., 2018. Biosens. Bioelectron. 101, 159–166.
Zhang, N., Ciriminna, R., Pagliaro, M., Xu, Y., 2014. Chem. Soc. Rev. 43, 5276–5287.
Zhao, Q., Liu, L., Li, S., Liu, R., 2019. Appl. Surf. Sci. 465, 164–171.
Zhao, W., Xu, J., Chen, H., 2015. Chem. Soc. Rev. 44, 729–741.
Zhou, Q., Lin, Y., Zhang, K., Li, M., Tang, D., 2018. Biosens. Bioelectron. 101, 146–152.
Zhuo, Y., Huang, J., Cao, L., Ouyang, H., Wu, J., 2013. Mater. Lett. 90, 107–110.